NANO LETTERS

pubs.acs.org/NanoLett

Letter

Polychromatic Dual-Mode Imaging with Structured Chiral Photonic Crystals

Dong Zhu, Yi-Heng Zhang, Si-Jia Liu, Wen Chen, Lin Zhu, Shi-Jun Ge, Peng Chen,* Wei Duan,* and Yan-Qing Lu*

Cite This: *Nano Lett.* 2024, 24, 140−147

Read Online

ACCESS | Metrics & More | Article Recommendations

ABSTRACT: Optical spatial differentiation is a typical operation of optical analog computing and can single out the edge to accelerate the subsequent image processing, but in some cases, overall information about the object needs to be presented synchronously. Here, we propose a multifunctional optical device based on structured chiral photonic crystals for the simultaneous realization of real-time dual-mode imaging. This optical differentiator is realized by self-organized large-birefringence cholesteric liquid crystals, which are photopatterned to encode with a special integrated geometric phase. Two highly spin-selective modes of second-order spatial differentiation and bright-field imaging are exhibited in the reflected and transmitted directions, respectively. Two-dimensional edges of both amplitude and phase objects have been efficiently enhanced in high contrast and the broadband spectrum. This work extends the ingenious building of hierarchical chiral nanostructures, enriches their applications in the emerging frontiers of optical computing, and boasts considerable potential in machine vision and microscopy.

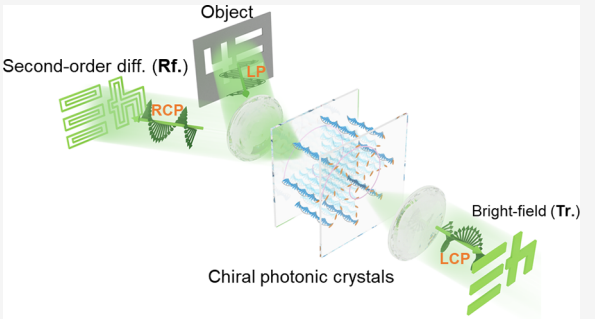

KEYWORDS: *optical spatial differentiation, cholesteric liquid crystals, edge detection, chiral photonic crystals, geometric phases*

Image processing plays a central role in diverse fields, especially in machine vision,[1] autonomous vehicles,[2] and microscopy.[3,4] In practice, the edges of an object, including amplitude object and phase object, preserve the most valuable information. Therefore, edge detection, namely spatial differentiation, can greatly decrease the amount of data to be processed.[5] In addition to digital image processing methods, the diffraction of light actually offers a natural platform for implementing various kinds of analog computations, like Fourier transform and convolution. The desired optical edge detection can be achieved by appropriate wavefront-shaping components like metasurfaces[6−9] and spatial light modulators.[10,11] Phase contrast imaging[12−14] and differential interference contrast imaging[15] are two typical methods. They have been successfully used to highlight the edges and reveal the geometric shapes of undyed cells. Compared with circuit-based digital computing, optical analog computing can present the result in a much faster and more efficient way.[16,17] However, when it comes to complex object recognition such as living cell migration imaging, the real-time entire morphology of the sample is also required,[18,19] making it important to realize edge detection and bright-field imaging at the same time.

As a typical liquid crystalline mesophase, cholesteric liquid crystals (CLCs) exhibit appealing properties[20−22] that derive from the ingenious helical arrangement of rod-like molecules and have exhibited great potential in optical field control.[23−26] The birefringence of the molecular units and the chirality of the self-assembled structure give rise to a chiral photonic band gap (PBG) in CLCs,[27] analogous to a one-dimensional photonic crystal. When the wavelength falls into the PBG, the circularly polarized light whose handedness matches the CLC chirality is strongly reflected, while the opposite circular polarization is transmitted and propagates along the initial direction. Notably, in this anisotropic and chiral nanoarchitecture, the spin−orbit interaction introduces an extra geometric phase[23,28,29] (i.e., Pancharatnam−Berry phase) in the reflected light, while the transmitted light remains unmodulated. If such a spin-dependent propagating direction and spin-selective light manipulation are fully exploited, synchronous spatial differentiation and bright-field imaging could be realized in a desired manner.

In this work, we propose a multifunctional optical operator for the simultaneous realization of two-dimensional (2D)

Received: September 8, 2023
Revised: November 15, 2023
Accepted: November 15, 2023
Published: November 20, 2023

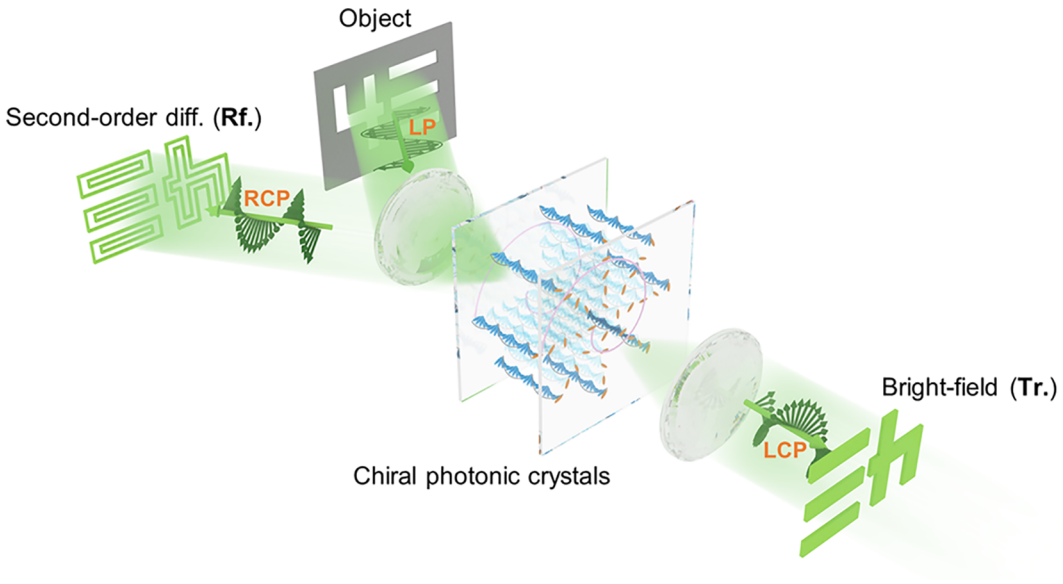

Figure 1. Schematic of the structured chiral photonic crystals for simultaneously realizing second-order spatial differentiation (diff.) and bright-field imaging. When a linearly polarized (LP) light is incident on this multifunctional optical operator, the right circularly polarized (RCP) light component will be reflected (Rf.) and performed with the second-order differentiation operation, while the left circularly polarized (LCP) light component will be transmitted (Tr.) and preserve the intensity profile as the initial object. The blue rods are the LC molecules, and the gray lines show the right handedness of their helical arrangement. The orange rods at the substrates indicate the LC director's orientation distribution at the surface. The pink line like Archimedean spiral marks the LC molecules whose orientation angles are equal to zero. The dark green arrows indicate the instantaneous spatial electric field of light.

second-order spatial differentiation and bright-field imaging (Figure 1). This optical differentiator is fabricated by photopatterning self-organized CLC chiral photonic crystals. To perform second-order spatial differentiation, a spiral phase integrated with a radial gradient phase is designed and encoded into the surface director orientations of CLC superstructures. A large-birefringence liquid crystal (LC) is introduced to enable a broadband operating spectrum. For an amplitude object, polychromatic second-order edge detection and bright-field imaging are synchronously demonstrated in a polarization-selective way with good quality. For a phase object made of nematic LC, dual-mode imaging is also well verified with the merits of high contrast and high efficiency. The proposed differentiator provides an innovative method for object recognition and has broad prospects in the fields of optical imaging and information processing.

We use the Berreman's 4 × 4 matrix method[30] to analyze the optical properties of CLC chiral photonic crystals under normal incidence. For the right-handed CLCs (Figure 2a,b), owing to the Bragg reflection, the reflectance of RCP is approximately 100% within the wavelength range from n_0p to n_ep (i.e., the PBG), where n_0 and n_e are the ordinary and extraordinary refractive indices, respectively, and p is the helical pitch. The spatially variant CLC's director orientation α (inset in Figure 2e) endows the reflected RCP light with a geometric phase $\varphi = +2\alpha$.[23,31] For the LCP component of the incident light, this right-handed chiral nanostructure behaves like a homogeneous dielectric medium, so that all LCP light passes with a uniform dynamic phase shift independent of α.[32]

We superimpose a spiral phase with the topological charge $m = +1$ and a radial gradient phase with a large period $T = 850$ μm and encode this integrated phase profile in the surface director orientations of the CLCs (Figure 2c,d). The corresponding reflective geometric phase attached to the RCP light is given by

$$\varphi(x, y) = \theta + \frac{2\pi}{T}r \tag{1}$$

where (r, θ) represents the polar coordinates. The proposed device is placed at the Fourier plane of the 4-F system and works as a spatial filter in the spatial frequency domain. The output of the whole system, $E_{out}(x, y)$, is equivalent to the convolution of input $E_{in}(x, y)$ and point spread function (PSF) $h(x, y)$, as follows

$$E_{out}(x, y) = E_{in}(x, y) \otimes h(x, y) \tag{2}$$

$h(x, y)$ can be written as the inverse Fourier transform of transfer function $H(x, y)$. For the transmitted imaging mode, the transfer function can be treated as a constant function so that the output is just identical to the input. For the reflected imaging mode, the transfer function depends on our designed CLC structures, following the equation $H(x, y) = \exp[i(\theta + 2\pi \times \lambda f r/T)]$. Acting as the scale factors, λ is the wavelength of the incident light and f is the focal length of the lens.

In our superimposed phase structure, the carefully designed radial gradient phase introduces extra effects beyond the common spiral phase (i.e., radial Hilbert transform[12]). Because $T/(\lambda f)$ is large enough, we can approximately employ the first-order Taylor expansion in the reflected transfer function as

$$H(x, y) \approx e^{i\theta} - i\frac{2\pi}{T}\lambda f r \times e^{i\theta} \approx H_1(x, y) - H_2(x, y) \tag{3}$$

Because of the linearity of the 4-F system, the final output can be seen as the interference between the corresponding outputs of the two parts presented above, which are expressed as E_{out1} and E_{out2}, respectively. The first part $H_1(x, y)$ just presents the spiral phase contrast imaging and corresponds to differentiation operation $\partial/\partial x + i\partial/\partial y$.[33,34] For the second part, $H_2(x, y)$, the function of $ir\exp(i\theta)$ is equivalent to partial differentiation operation $\partial/\partial x + i\partial/\partial y$ after the Fourier

https://doi.org/10.1021/acs.nanolett.3c03437
Nano Lett. 2024, 24, 140−147

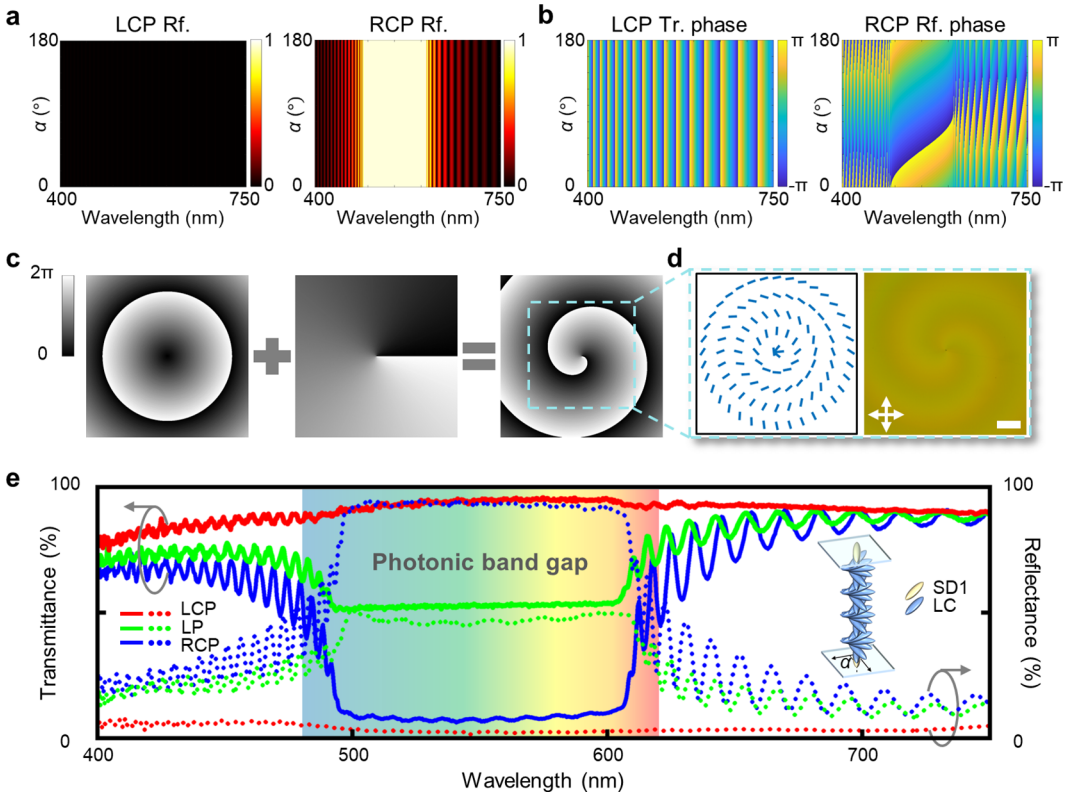

Figure 2. Simulated results, designed phase pattern, and experimental transmittance and reflectance spectra of the CLC differentiator. (a) Simulated reflection for the LCP and RCP incident light at different wavelengths and orientation angles. The color bars illustrate the reflectance. (b) Simulated relative phase for the transmitted LCP light and reflected RCP light at different wavelengths and orientation angles. The color bars indicate the value of the endowed phase. (c) The designed phase pattern is the superposition of the radial gradient phase and the spiral phase. (d) Theoretical surface director distribution and reflective micrograph of the CLC device corresponding to the region marked in panel c. The orthogonal white arrows indicate the crossed polarizer and analyzer of the optical microscope. The scale bar is 200 μm. (e) Experimental transmittance and reflectance spectra for different polarized light. The PBG is marked with the corresponding color. The inset shows the right-handed CLC nanostructure, where α is the orientation angle of the LC director on the substrates.

transform.[35] These mean both parts in eq 3 can contribute to the first-order spatial differentiation. In addition, their PSFs, $h_1(x, y)$ and $h_2(x, y)$, have similar features like the impulse function but have different radii, which will lead to a different broadening of the output. It finally influences the spatial magnification of E_{out1} and E_{out2} and results in first-order differentiation once again, which can be expressed as $E_{out1} - E_{out2} = \partial E_{out1}/\partial r$. Therefore

$$E_{out} \approx E_{out1} - E_{out2} \approx \left(\frac{\partial}{\partial x} + i\frac{\partial}{\partial y}\right)\frac{\partial E_{in}}{\partial r} \quad (4)$$

In brief, $E_{out}(x, y)$ demonstrates 2D second-order spatial differentiation of the object. Notably, period T is a key parameter and should be appropriately optimized to make sure that the approximation presented above has been well satisfied and meanwhile the phase structure does not degenerate to a simple spiral phase. As vividly shown in Figure 1, the RCP component of the incident light is reflected, and the corresponding output is an isotropic second-order spatial differential image. On the contrary, the LCP component is transmitted and its intensity distribution is the same as that of the object, contributing to the bright-field imaging.

To imprint the integrated phase pattern presented above (Figure 2c) on the CLC chiral superstructures, a polarization-sensitive photoalignment agent (sulfonic azo-dye SD1, DIC) is spin-coated on the substrates, which will reorient its absorption oscillator perpendicular to the polarization of the illuminated ultraviolet (UV) light. Using a digital micromirror device as a dynamic mask,[36,37] the LC director's orientation is well encoded under the spatially variant polarized UV exposure. To achieve a CLC differentiator with a broad operating spectrum, a large-birefringence nematic host (TD101−146; Δn = 0.402; HCCH) is introduced and mixed with 2.83 wt % right-handed chiral dopant R5011 (HCCH). After filling the photopatterned cell, all LC molecules are self-assembled to form the designed chiral photonic structures under the guidance of surface anchoring. Figure 2d shows the theoretical surface LC director distribution and the reflective micrograph of the fabricated sample under a polarized optical microscope. The transmittance and reflectance spectra of this CLC differentiator are measured under LCP, RCP, and LP incidence (Figure 2e). A polarization-selective and broadband PBG ranging from 480 to 620 nm is clearly revealed, which covers almost from blue to red and is consistent with the simulation results in Figure 2a.

This structured chiral photonic crystal is further mounted at the focal plane of the 4-F system and serves as a spatial filter, whose PSF is numerically simulated, as shown in Figure 3a. The amplitude of the PSF is composed of two main donut-shaped functions, which are $h_1(x, y)$ and $h_2(x, y)$, while the corresponding phase profile indicates a multiplied spiral phase. The experimental setup for the verification of the fabricated CLC differentiator is schematically illustrated in Figure 3b. A

https://doi.org/10.1021/acs.nanolett.3c03437
Nano Lett. 2024, 24, 140−147

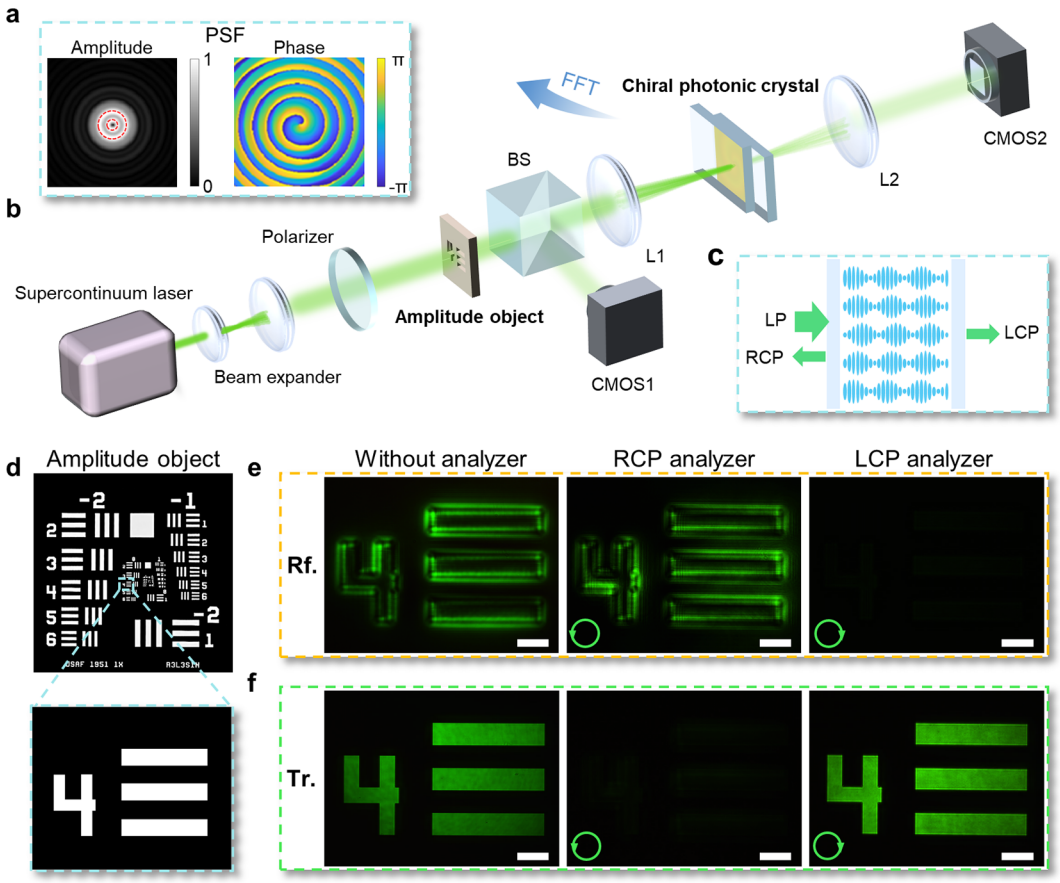

Figure 3. PSF, optical setup, and spin-selective dual-mode imaging results for the amplitude object using the proposed multifunctional differentiator. (a) Numerical calculation result of the PSF. (b) Sketch of the experimental optical setup. Abbreviations: BS, nonpolarizing beam splitter; L, achromatic lens; FFT, fast Fourier transform. (c) Schematic of the spin selectivity of the structured chiral photonic crystals. (d) 1951 USAF resolution test chart. The region enlarged inside the dashed line is used as the amplitude object for detection. (e and f) Reflected and transmitted output images, respectively, captured by CMOS cameras under different circular polarization analyzers. The green circular arrows represent the handedness of the analyzed polarization. All scale bars are 500 μm.

supercontinuum laser emits a monochromatic Gauss beam with the aid of a multichannel acousto-optic tunable filter. After propagating through a beam expander and a linear polarizer, the incident light uniformly illuminates the observed object, which is placed in the front focal plane of the first achromatic lens. Because the CLC device presents a strong spin-determined reflection (Figure 3c), it will introduce a confocal configuration into the traditional 4-F system. Specifically, the reflected RCP light is modulated by the reflective geometric phase of CLCs and passes through the first lens twice along with the Fourier transform, resulting in a distinct edge image at the object position. By inserting a nonpolarizing beam splitter, one can send the corresponding output light patterns to a CMOS camera on the other side. Meanwhile, the transmitted LCP component just experiences a uniform phase shift within CLCs. After passing through the second achromatic lens, the bright-field image that includes overall information about the initial object is recorded by another CMOS camera.

First, the 1951 USAF resolution test chart is chosen as a representative example of the amplitude object (Figure 3d). Element 4 of group 0, including a series of horizontal lines and a number, is illuminated, and the resolution is 0.71 mm per line pair. Panels e and f of Figure 3 show the experimental imaging results of this test target at a wavelength of 545 nm. In the reflected pattern, the double adjacent intensity maxima are evidently located near the edge of the amplitude object without obvious zeroth-order diffraction, which credibly verifies the 2D second-order spatial differentiation in a high-efficiency and high-quality way, while the transmitted light preserves the input, indicating bright-field imaging. Moreover, we analyze the output polarization in two modes by a quarter-wave plate and a linear polarizer. Both imaging modes possess nearly pure circular polarization, and the spin-selective nature of this chiral optical differentiator is well proved. These results verify that the proposed CLC device can synchronously realize dual-mode imaging without any observable cross-talk, and the imaging mode can be easily switched by changing the incident polarization. Compared with that of common first-order differentiation, the resolution of second-order optical differentiation is relatively lower and can be further improved using a higher-resolution LC photopatterning technique and by properly enlarging the numerical aperture of lenses in the optical setup.

The PBG of this chiral photonic crystal is from blue to red (Figure 2e), indicating a wide operating wavelength range. To validate the broadband capability of this CLC device, the incident wavelength is filtered at 505, 545, 580, 595, and 620 nm. Because the reflective geometric phase modulation is determined by the spatially variant CLC structures and

https://doi.org/10.1021/acs.nanolett.3c03437
Nano Lett. 2024, 24, 140−147

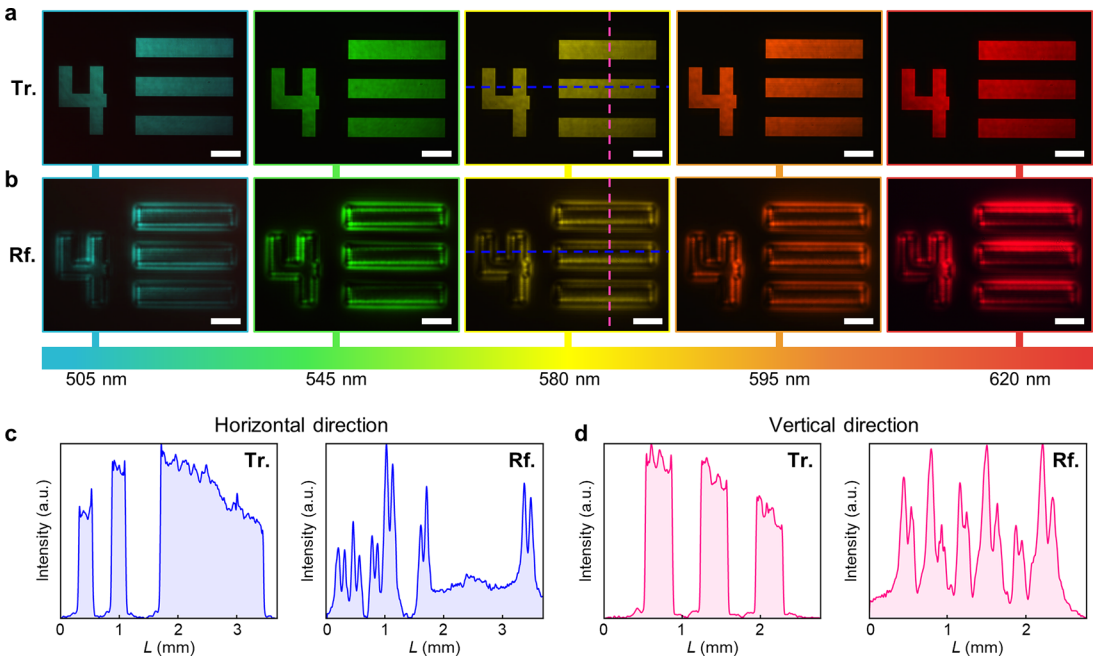

Figure 4. Polychromatic dual-mode imaging based on the structured chiral photonic crystal. (a) Transmitted images and (b) reflected images at incident wavelengths of 505, 545, 580, 595, and 620 nm. All scale bars are 500 μm. (c) Blue and (d) pink intensity curves correspond to the horizontal and vertical dashed lines in panels a and b, respectively.

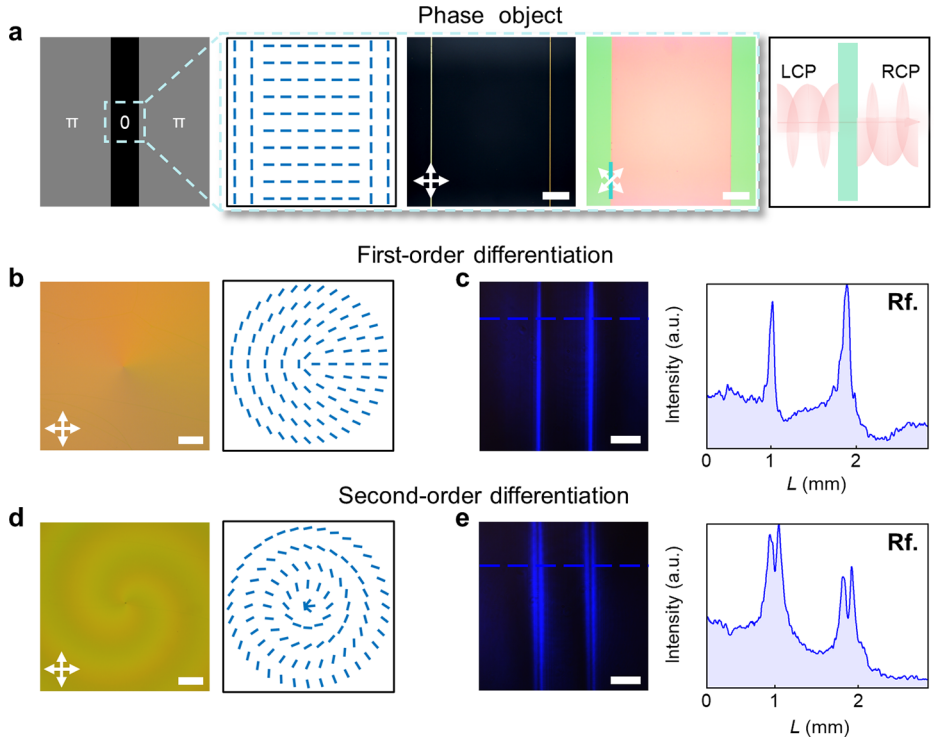

Figure 5. LC phase object and corresponding first- and second-order differentiation. (a) Designed binary phase object made of nematic LCs. Two gray levels indicate the binary geometric phases 0 and π. The theoretical LC director distribution and two micrographs correspond to the marked region. The cyan bar indicates the full-wave plate at 530 nm as the sensitive tint plate for distinguishing the orthogonal LC directors. Scale bars are 200 μm. The right diagram exhibits the inversion of the circular polarization under the half-wave condition of the fabricated LC phase mask. (b and d) Micrographs and theorical LC director distributions of the spiral phase device with topological charge m = 1 and the proposed phase-integrated device. Scale bars are 200 μm. (c and e) First- and second-order spatial differential images at 480 nm with marked intensity curves. Scale bars are 500 μm.

independent of the wavelength within PBG, the efficiency and the transfer function of the fabricated differentiator should be basically consistent. As a result, the intensity distributions of dual-mode images within PBG will stay the same without the necessity of adjusting the optical setup. Panels a and b of Figure 4 show the experimental transmitted bright-field images

https://doi.org/10.1021/acs.nanolett.3c03437
Nano Lett. 2024, 24, 140−147

and the reflected second-order spatial differentiation images, respectively, at various wavelengths, which keep almost the same resolution, efficiency, and contrast over such a wide spectrum. The one-dimensional section of the intensity distribution along the horizontal blue and vertical pink dashed lines is shown in panels c and d of Figure 4. We have verified that the edge information on the amplitude object can be isotropically highlighted in a polychromatic and high-quality manner.

In addition to the amplitude object, the identification of a phase object is also greatly significant. A phase object without any amplitude modulation for light can barely be recognized by the human eye, which raises formidable challenges for extracting effective information about its morphology and fine internal structures. Typical cases include the most frequently investigated biological cells without natural pigments[8,15] and transparent anisotropic materials like the LC microstructures. Here, we further design a binary phase object based on nematic LCs (Figure 5a) to verify the phase edge detection capability of our proposed CLC differentiator. The nematic LC object is essentially a half-wave plate composed of three subareas, whose local optical axes (i.e., LC directors) are aligned at 90°, 0°, and 90° (Figure 5a). For LCP incidence, the transmitted light becomes RCP, along with the geometric phase modulation dependent on the nematic LC orientation angle.[24,38] Accordingly, a binary phase mask with 0 and π is obtained. Moreover, to vividly demonstrate the distinction between different order differentiation operators, we also fabricate a CLC spiral phase plate with the topological charge $m = +1$ (Figure 5b), without any radial gradient. Panels c and e of Figure 5 show the experimental results of these two kinds of edge detection at 480 nm. The CLC spiral phase plate operates the first-order differentiation by enhancing just one intensity maximum in the neighborhood of the phase edge, while the proposed CLC device (Figure 5d) produces two adjacent intensity maxima near the phase edge, corresponding to second-order differentiation. This second-order spatial differentiator can highlight the phase mutation points of the first-order derivative and serves as a more sensitive indicator of object variation, which has great potential in more accurately tracking edges and revealing new fine details.[39,40]

In conclusion, we propose and demonstrate an innovative optical differentiator that uses structured chiral photonic crystals. The carefully designed integrated phase profile is encoded into self-assembled CLCs by photopatterning. A dual imaging mode, including 2D second-order spatial differentiation and bright-field imaging, can be simultaneously realized with sensitive polarization dependence, high efficiency, and high quality. The edge information about both the amplitude object and the phase object is successfully identified with a broadband operating spectrum. To further integrate the optical setup into one-side imaging, bi-chiral CLC nanostructures,[37] which can reflect all polarization components and endow different geometric phases into orthogonal circular polarization, can be programmed to perform dual-mode imaging only in the reflection side. Compared with multifunctional optical differentiators based on metasurfaces, our proposed CLC device has unique superiorities of fast molecular self-assembly and high modulation efficiency, which is exempt from any sophisticated and expensive nanofabrication process. In addition, CLCs are featured by the versatile stimulus-responsive characteristics,[24,36] so the dynamic tunability of the dual-mode imaging can be rationally expected. This work promotes an efficient method for application in machine vision and microscopy and provides new opportunities of soft chiral superstructures in the frontiers of optical analog computing for artificial intelligence.

AUTHOR INFORMATION

Corresponding Authors

Peng Chen − *National Laboratory of Solid State Microstructures, Key Laboratory of Intelligent Optical Sensing and Manipulation, College of Engineering and Applied Sciences, and Collaborative Innovation Center of Advanced Microstructures, Nanjing University, Nanjing 210093, China*; orcid.org/0000-0003-3559-8359; Email: chenpeng@nju.edu.cn

Wei Duan − *School of Instrumentation and Optoelectronic Engineering, Beihang University, Beijing 100191, China*; Email: wduan@buaa.edu.cn

Yan-Qing Lu − *National Laboratory of Solid State Microstructures, Key Laboratory of Intelligent Optical Sensing and Manipulation, College of Engineering and Applied Sciences, and Collaborative Innovation Center of Advanced Microstructures, Nanjing University, Nanjing 210093, China*; orcid.org/0000-0001-6151-8557; Email: yqlu@nju.edu.cn

Authors

Dong Zhu − *National Laboratory of Solid State Microstructures, Key Laboratory of Intelligent Optical Sensing and Manipulation, College of Engineering and Applied Sciences, and Collaborative Innovation Center of Advanced Microstructures, Nanjing University, Nanjing 210093, China*

Yi-Heng Zhang − *National Laboratory of Solid State Microstructures, Key Laboratory of Intelligent Optical Sensing and Manipulation, College of Engineering and Applied Sciences, and Collaborative Innovation Center of Advanced Microstructures, Nanjing University, Nanjing 210093, China*

Si-Jia Liu − *National Laboratory of Solid State Microstructures, Key Laboratory of Intelligent Optical Sensing and Manipulation, College of Engineering and Applied Sciences, and Collaborative Innovation Center of Advanced Microstructures, Nanjing University, Nanjing 210093, China*

Wen Chen − *National Laboratory of Solid State Microstructures, Key Laboratory of Intelligent Optical Sensing and Manipulation, College of Engineering and Applied Sciences, and Collaborative Innovation Center of Advanced Microstructures, Nanjing University, Nanjing 210093, China*

Lin Zhu − *National Laboratory of Solid State Microstructures, Key Laboratory of Intelligent Optical Sensing and Manipulation, College of Engineering and Applied Sciences, and Collaborative Innovation Center of Advanced Microstructures, Nanjing University, Nanjing 210093, China*

Shi-Jun Ge − *National Laboratory of Solid State Microstructures, Key Laboratory of Intelligent Optical Sensing and Manipulation, College of Engineering and Applied Sciences, and Collaborative Innovation Center of Advanced Microstructures, Nanjing University, Nanjing 210093, China*; orcid.org/0000-0002-2493-0347

Complete contact information is available at: https://pubs.acs.org/10.1021/acs.nanolett.3c03437

Author Contributions

P.C., D.Z., and Y.-Q.L. conceived the original idea and designed the experiment. D.Z. conducted the designs,

https://doi.org/10.1021/acs.nanolett.3c03437
Nano Lett. 2024, 24, 140−147

performed the experiments, and analyzed the data with the assistance of Y.-H.Z., S.-J.L., W.C., L.Z., S.-J.G., and W.D. D.Z. and P.C. prepared the original manuscript. All authors participated in the discussion and contributed to revision of the manuscript. P.C., W.D., and Y.-Q.L. co-supervised and directed the research.

Notes

The authors declare no competing financial interest.

■ ACKNOWLEDGMENTS

This work was supported by the National Key R&D Program of China (2021YFA1202000, and 2022YFA1203700), the National Natural Science Foundation of China (NSFC) (62222507, 12004175, 62175101, and 62005009), the Innovation Program for Quantum Science and Technology (2021ZD0301500), and the Natural Science Foundation of Jiangsu Province (BK20212004 and BK20200311).

■ REFERENCES

(1) Yuan, S. F.; Ma, C.; Fetaya, E.; Mueller, T.; Naveh, D.; Zhang, F.; Xia, F. N. Geometric deep optical sensing. *Science* **2023**, *379* (6637), No. eade1220.
(2) Bao, F. L.; Wang, X. J.; Sureshbabu, S. H.; Sreekumar, G.; Yang, L. P.; Aggarwal, V.; Boddeti, V. N.; Jacob, Z. Heat-assisted detection and ranging. *Nature* **2023**, *619* (7971), 743−748.
(3) Zernike, F. Phase contrast, a new method for the microscopic observation of transparent objects. *Physica* **1942**, *9* (7), 686−698.
(4) Vicidomini, G.; Bianchini, P.; Diaspro, A. STED super-resolved microscopy. *Nat. Methods* **2018**, *15* (3), 173−182.
(5) He, S. S.; Wang, R. S.; Luo, H. L. Computing metasurfaces for all-optical image processing: a brief review. *Nanophotonics* **2022**, *11* (6), 1083−1108.
(6) Zhu, T. F.; Zhou, Y. H.; Lou, Y. J.; Ye, H.; Qiu, M.; Ruan, Z. C.; Fan, S. H. Plasmonic computing of spatial differentiation. *Nat. Commun.* **2017**, *8*, 15391.
(7) Zhou, J. X.; Qian, H. L.; Chen, C. F.; Zhao, J. X.; Li, G. R.; Wu, Q. Y.; Luo, H. L.; Wen, S. C.; Liu, Z. W. Optical edge detection based on high-efficiency dielectric metasurface. *Proc. Natl. Acad. Sci. U.S.A.* **2019**, *116* (23), 11137−11140.
(8) Zhou, Y.; Zheng, H. Y.; Kravchenko, I. I.; Valentine, J. Flat optics for image differentiation. *Nat. Photonics* **2020**, *14* (5), 316−323.
(9) Intaravanne, Y.; Ansari, M. A.; Ahmed, H.; Bileckaja, N.; Yin, H. B.; Chen, X. Z. Metasurface-enabled 3-in-1 microscopy. *ACS Photonics* **2023**, *10* (2), 544−551.
(10) Jesacher, A.; Fürhapter, S.; Bernet, S.; Ritsch-Marte, M. Shadow effects in spiral phase contrast microscopy. *Phys. Rev. Lett.* **2005**, *94* (23), 233902.
(11) Qiu, X. D.; Li, F. S.; Zhang, W. H.; Zhu, Z. H.; Chen, L. X. Spiral phase contrast imaging in nonlinear optics: seeing phase objects using invisible illumination. *Optica* **2018**, *5* (2), 208−212.
(12) Davis, J. A.; McNamara, D. E.; Cottrell, D. M.; Campos, J. Image processing with the radial Hilbert transform: theory and experiments. *Opt. Lett.* **2000**, *25* (2), 99−101.
(13) Zhao, M. T.; Liang, X. Z.; Li, J. S.; Xie, M. Y.; Zheng, H. D.; Zhong, Y. C.; Yu, J. H.; Zhang, J.; Chen, Z.; Zhu, W. G. Optical phase contrast microscopy with incoherent vortex phase. *Laser Photonics Rev.* **2022**, *16* (11), 2200230.
(14) Huo, P. C.; Zhang, C.; Zhu, W. Q.; Liu, M. Z.; Zhang, S.; Zhang, S.; Chen, L.; Lezec, H. J.; Agrawal, A.; Lu, Y. Q.; Xu, T. Photonic spin-multiplexing metasurface for switchable spiral phase contrast imaging. *Nano Lett.* **2020**, *20* (4), 2791−2798.
(15) Wang, X. W.; Wang, H.; Wang, J. L.; Liu, X. S.; Hao, H. J.; Tan, Y. S.; Zhang, Y. L.; Zhang, H.; Ding, X. Y.; Zhao, W. S.; Wang, Y. H.; Lu, Z. G.; Liu, J.; Yang, J. K. W.; Tan, J. B.; Li, H. Y.; Qiu, C. W.; Hu, G. W.; Ding, X. M. Single-shot isotropic differential interference contrast microscopy. *Nat. Commun.* **2023**, *14*, 2063.
(16) Solli, D. R.; Jalali, B. Analog optical computing. *Nat. Photonics* **2015**, *9* (11), 704−706.
(17) Liu, S. Q.; Fan, F.; Chen, S. Z.; Wen, S. C.; Luo, H. L. Computing liquid-crystal photonics platform enabled wavefront sensing. *Laser Photonics Rev.* **2023**, *17* (8), 2300044.
(18) Zhang, Y. Z.; Lin, P. C.; Huo, P. C.; Liu, M. Z.; Ren, Y. Z.; Zhang, S.; Zhou, Q. W.; Wang, Y. L.; Lu, Y. Q.; Xu, T. Dielectric metasurface for synchronously spiral phase contrast and bright-field imaging. *Nano Lett.* **2023**, *23* (7), 2991−2997.
(19) Badloe, T.; Kim, Y.; Kim, J.; Park, H.; Barulin, A.; Diep, Y. N.; Cho, H.; Kim, W. S.; Kim, Y. K.; Kim, I.; Rho, J. Bright-field and edge-enhanced imaging using an electrically tunable dual-mode metalens. *ACS Nano* **2023**, *17* (15), 14678−14685.
(20) Bisoyi, H. K.; Li, Q. Liquid crystals: versatile self-organized smart soft materials. *Chem. Rev.* **2022**, *122* (5), 4887−4926.
(21) Schwartz, M.; Lenzini, G.; Geng, Y.; Rønne, P. B.; Ryan, P. Y. A.; Lagerwall, J. P. F. Cholesteric liquid crystal shells as enabling material for information-rich design and architecture. *Adv. Mater.* **2018**, *30* (30), 1707382.
(22) Cao, Y.; Chong, L.; Wu, K. H.; You, L. Q.; Li, S. S.; Chen, L. J. Dynamic coloration of polymerized cholesteric liquid crystal networks by infiltrating organic compounds. *Chin. Opt. Lett.* **2022**, *20* (9), 091602.
(23) Kobashi, J.; Yoshida, H.; Ozaki, M. Planar optics with patterned chiral liquid crystals. *Nat. Photonics* **2016**, *10* (6), 389−392.
(24) Chen, P.; Wei, B. Y.; Hu, W.; Lu, Y. Q. Liquid-crystal-mediated geometric phase: from transmissive to broadband reflective planar optics. *Adv. Mater.* **2020**, *32* (27), 1903665.
(25) Xiong, J. H.; Yang, Q.; Li, Y. N.; Wu, S. T. Holo-imprinting polarization optics with a reflective liquid crystal hologram template. *Light: Sci. Appl.* **2022**, *11*, 54.
(26) Zhu, L.; Xu, C. T.; Chen, P.; Zhang, Y. H.; Liu, S. J.; Chen, Q. M.; Ge, S. J.; Hu, W.; Lu, Y. Q. Pancharatnam-Berry phase reversal via opposite-chirality-coexisted superstructures. *Light: Sci. Appl.* **2022**, *11*, 135.
(27) Faryad, M.; Lakhtakia, A. The circular Bragg phenomenon. *Adv. Opt. Photonics* **2014**, *6* (2), 225−292.
(28) Rafayelyan, M.; Tkachenko, G.; Brasselet, E. Reflective spin-orbit geometric phase from chiral anisotropic optical media. *Phys. Rev. Lett.* **2016**, *116* (25), 253902.
(29) Barboza, R.; Bortolozzo, U.; Clerc, M. G.; Residori, S. Berry phase of light under Bragg reflection by chiral liquid-crystal media. *Phys. Rev. Lett.* **2016**, *117* (5), 053903.
(30) Berreman, D. W. Optics in stratified and anisotropic media: 4 × 4-matrix formulation. *J. Opt. Soc. Am.* **1972**, *62* (4), 502−510.
(31) Chen, P.; Shen, Z. X.; Xu, C. T.; Zhang, Y. H.; Ge, S. J.; Ma, L. L.; Hu, W.; Lu, Y. Q. Simultaneous realization of dynamic and hybrid multiplexed holography via light-activated chiral superstructures. *Laser Photonics Rev.* **2022**, *16* (5), 2200011.
(32) Chen, P.; Ma, L. L.; Duan, W.; Chen, J.; Ge, S. J.; Zhu, Z. H.; Tang, M. J.; Xu, R.; Gao, W.; Li, T.; Hu, W.; Lu, Y. Q. Digitalizing self-assembled chiral superstructures for optical vortex processing. *Adv. Mater.* **2018**, *30* (10), 1705865.
(33) Zhu, T. F.; Guo, C.; Huang, J. Y.; Wang, H. W.; Orenstein, M.; Ruan, Z. C.; Fan, S. H. Topological optical differentiator. *Nat. Commun.* **2021**, *12*, 680.
(34) Xu, D. Y.; Yang, H.; Xu, W. H.; Zhang, W. S.; Zeng, K. M.; Luo, H. L. Inverse design of Pancharatnam-Berry phase metasurfaces for all-optical image edge detection. *Appl. Phys. Lett.* **2022**, *120* (24), 241101.
(35) Goodman, J. W. *Introduction to Fourier Optics*, 3rd ed.; Roberts & Company Publishers: Englewood, CO, 2005.
(36) Chen, P.; Ma, L. L.; Hu, W.; Shen, Z. X.; Bisoyi, H. K.; Wu, S. B.; Ge, S. J.; Li, Q.; Lu, Y. Q. Chirality invertible superstructure mediated active planar optics. *Nat. Commun.* **2019**, *10*, 2518.
(37) Liu, S. J.; Zhu, L.; Zhang, Y. H.; Chen, W.; Zhu, D.; Chen, P.; Lu, Y. Q. Bi-chiral nanostructures featuring dynamic optical rotatory dispersion for polychromatic light multiplexing. *Adv. Mater.* **2023**, *35* (33), 2301714.

https://doi.org/10.1021/acs.nanolett.3c03437
Nano Lett. 2024, 24, 140−147

(38) Jisha, C. P.; Nolte, S.; Alberucci, A. Geometric phase in optics: from wavefront manipulation to waveguiding. *Laser Photonics Rev.* **2021**, *15* (10), 2100003.
(39) Liu, Y.; Huang, M. C.; Chen, Q. K.; Zhang, D. G. Single planar photonic chip with tailored angular transmission for multiple-order analog spatial differentiator. *Nat. Commun.* **2022**, *13*, 7944.
(40) Liang, X.; Zhou, Z.; Li, Z. L.; Li, J. X.; Peng, C.; Cui, H.; Wei, K.; He, Z. X.; Yu, S. H.; Zheng, G. X. All-optical multiplexed meta-differentiator for tri-mode surface morphology observation. *Adv. Mater.* **2023**, *35* (29), 2301505.

https://doi.org/10.1021/acs.nanolett.3c03437
Nano Lett. 2024, 24, 140−147